Ab initio study of electron energy loss spectra of bulk bismuth up to 100 eV

Iurii Timrov,[1,2,*] Maxime Markov,[1] Tommaso Gorni,[2] Michèle Raynaud,[1] Oleksandr Motornyi,[1] Ralph Gebauer,[3,4] Stefano Baroni,[2,4] and Nathalie Vast[1]

[1]*Laboratoire des Solides Irradiés, École Polytechnique - CEA/DRF - CNRS UMR 7642, 91128 Palaiseau cédex, France*

[2]*Scuola Internazionale Superiore di Studi Avanzati (SISSA), Via Bonomea 265, IT-34136 Trieste, Italy*

[3]*The Abdus Salam International Centre for Theoretical Physics (ICTP), Strada Costiera 11, IT-34151 Trieste, Italy*

[4]*CNR-IOM DEMOCRITOS Simulation Center, IT-34136 Trieste, Italy*

(Received 2 August 2016; revised manuscript received 9 December 2016; published 1 March 2017)

The dynamical charge-density response of bulk bismuth has been studied within time-dependent density functional perturbation theory, explicitly accounting for spin-orbit coupling. The use of the Liouville–Lanczos approach allows us to calculate electron energy loss spectra for excitation energies as large as 100 eV. Effects of 5*d* semicore electronic states, spin-orbit coupling, exchange and correlation, local fields, and anisotropy are thoroughly investigated. The account of the 5*d* states in the calculation turns out to be crucial to correctly describe the loss spectra above 10 eV and, in particular, the position and shape of the bulk-plasmon peak at 14.0 eV at vanishing transferred momentum. Our calculations reveal the presence of interband transitions at 16.3 eV, which had never been discussed before. The origin of the peak at 5.8 eV is revisited as due to mixed interband and collective excitations. Finally, our study supplements the lack of experiments at finite transferred momenta.

DOI: 10.1103/PhysRevB.95.094301

I. INTRODUCTION

Electron energy loss (EEL) spectroscopy in a transmission electron microscope is the experimental technique established in the early 1960s to probe (neutral) fluctuations of the electronic density induced by an electronic beam, and in particular plasma oscillations [1]. The energy loss of incoming-beam electrons is measured from the double-differential cross section, a quantity related to the imaginary part of the inverse of the dielectric function. On the other hand, time-dependent density functional theory (TDDFT) [2,3] in the adiabatic local density approximation offers the best compromise between computational cost and accuracy for the calculation of plasmons in cases where static excitonic effects are not essential [4]. However, its use within the plane-wave pseudopotential (PP) approach is limited to the description of low (valence) energy losses, and alternate methods are required to treat losses from the (deep) inner core [5–7].

The intermediate energy range—describing electronic excitations spanning up to hundred electronvolts—is associated with a considerable quantity of possible final (empty) states. Because including this big number of states in the calculation is hardly possible using standard methods, we have recently proposed the Liouville–Lanczos (LL) approach to EEL and inelastic x-ray scattering (IXS) spectroscopies [8–10]—a new approach which enables us to cover any extended energy range at a low computational cost. In this work, the LL method is applied to compute the electronic susceptibility of bismuth up to 100 eV, including excitations from 5*d* semicore states, and enables us to supplement the lack of experimental data for finite transferred momenta.

Bismuth (Bi) has the heaviest nucleus among group-V semimetals and requires a proper treatment of relativistic effects. Instead of solving nonrelativistic Kohn–Sham (KS) equations for scalar orbitals in combination with non- or semirelativistic PPs, one has to account for the large spin-orbit coupling (SOC) by solving Pauli-type KS equations for two-component spinor wave functions and use fully relativistic PPs. This theoretical problem is doubled by the computational difficulty to handle twice the number of electronic bands and, in fact, few studies including the effect of SOC have been reported so far [11–15]. A notable exception is provided by Refs. [13–15], which detail the effect of including both 5*d* semicore states and SOC when calculating the dielectric properties of lead.

The semimetallic character of the band structure of Bi, i.e., the tiny overlap between the highest valence band and the lowest conduction band, is due to the very large SOC, and it leads to many interesting phenomena: very large de Haas–van Alphen and Shubnikov–de Haas quantum oscillatory effects, thermoelectricity, excitations of coherent phonons [8,16]. Plasmon excitations have been less studied, and the effect of SOC on plasmons in Bi is unknown. At finite transferred momenta, EEL spectra have not been studied, neither theoretically nor experimentally. For vanishing transferred momentum, the EEL spectrum has been studied for bulk bismuth experimentally [17–23], and there is only one, to the best of our knowledge, theoretical study which was performed by using the random-phase approximation (RPA) [11]. More recently, Bi nanostructures were studied experimentally [24–29]. In this work we present a TDDFT study of the EEL spectra of bulk Bi in the wide (0–100 eV) energy range for vanishing transferred momentum and predict EEL spectra for various finite transferred momenta. We believe that our results will be helpful for future studies of bulk bismuth and its compounds and nanostructures.

The rest of this paper is organized as follows: In Sec. II we describe the computational method and provide numerical details of our calculations. In Secs. III and IV we present EEL spectra of Bi at vanishing and finite transferred momenta, respectively. Finally, Sec. V contains the conclusions, and the appendix recalls details of the band structure of Bi [8].

*Present address: Theory and Simulation of Materials (THEOS), École Polytechnique Fédérale de Lausanne, 1015 Lausanne, Switzerland.

II. COMPUTATIONAL METHOD

A. Link between experiment and theory

In an EEL experiment, incident electrons with wave vector $\mathbf{k}_i$ undergo an inelastic scattering due to Coulomb interaction with electrons and ions of the target sample [1]. They thus transfer to the target an energy $\hbar\omega$—observed as a loss of their kinetic energy—and a wave vector $\mathbf{Q} = \mathbf{k}_i - \mathbf{k}_f$, where $\mathbf{k}_f$ is the wave vector of the outcoming electron. The double-differential cross section describes how many incident electrons were scattered in the solid angle $d\Omega$ and transferred the energy $\hbar d\omega$ [30]:

$$\frac{d^2\sigma}{d\Omega d\omega} = -\frac{\hbar}{(\pi e a_0)^2}\frac{1}{Q^2}\mathrm{Im}[\epsilon^{-1}(\mathbf{Q},\omega)], \tag{1}$$

where $a_0 = \hbar^2/(m_0 e^2)$ is the Bohr radius, $-e$ is the electron charge, and m_0 is the free-electron mass. In periodic solids the transferred momentum can be presented as a sum of the wave vector in the first Brillouin zone (BZ) $\mathbf{q}$ and the reciprocal lattice vector $\mathbf{G}$: $\mathbf{Q} = \mathbf{q} + \mathbf{G}$. In Eq. (1), $\epsilon^{-1}(\mathbf{Q},\omega)$ is the inverse dielectric function which is the diagonal element of the inverse dielectric matrix, $\epsilon^{-1}(\mathbf{Q},\omega) \equiv \epsilon^{-1}(\mathbf{q}+\mathbf{G},\mathbf{q}+\mathbf{G};\omega)$, defined as [31,32]

$$\epsilon^{-1}(\mathbf{q}+\mathbf{G},\mathbf{q}+\mathbf{G}';\omega) = \delta_{\mathbf{G},\mathbf{G}'} + \frac{4\pi e^2}{|\mathbf{q}+\mathbf{G}|^2}\chi(\mathbf{q}+\mathbf{G},\mathbf{q}+\mathbf{G}';\omega), \tag{2}$$

where χ is the charge-density susceptibility, the poles of which correspond to plasmon frequencies and single-particle excitations.

For many systems, $\chi(\mathbf{Q},\mathbf{Q};\omega)$ can be conveniently and accurately computed by using TDDFT. Within the "conventional" approach one first computes the independent-particle polarizability, which involves the calculation of a large number of empty states, and then solves the Dyson-like screening integral equation in order to obtain the full susceptibility [4], which implies the inversion and multiplication of large matrices. Such a procedure must be repeated for each value of the frequency, which precludes its use for large energy ranges. While Bi can be studied by using such a "conventional" approach, we have used our recently proposed LL approach to EEL and IXS spectroscopies [8–10] within time-dependent density functional *perturbation* theory (TDDFpT) [33–35], which overcomes the drawbacks of the "conventional" approach and hence is more convenient for calculations of EEL spectra in the extended energy range.

B. Liouville–Lanczos approach within time-dependent density functional perturbation theory

In the LL approach, the frequency-dependent charge-density susceptibility for any given transferred momentum $\chi(\mathbf{Q},\mathbf{Q}';\omega)$ is expressed as the matrix element—diagonal with respect to $\mathbf{Q}$ and $\mathbf{Q}'$—of the resolvent of the Liouvillian $\hat{\mathcal{L}}$ of the system. The charge-density susceptibility describes the response of the monochromatic $\mathbf{Q}$ component of the charge-density operator, $\hat{n}_{\mathbf{Q}} \to e^{i\mathbf{Q}\cdot\mathbf{r}}$, to a monochromatic perturbation of the same wave vector, $\hat{V}_{\mathrm{ext},\mathbf{q}} = \hat{n}_{\mathbf{Q}}$; namely [8–10],

$$\chi(\mathbf{Q},\mathbf{Q};\omega) = (\hat{n}_{\mathbf{Q}}, (\hbar\omega - \hat{\mathcal{L}})^{-1}\cdot[\hat{n}_{\mathbf{Q}},\hat{\rho}^{\circ}]), \tag{3}$$

where $\hat{\rho}^{\circ}$ is the unperturbed density matrix, and $(\cdot,\cdot)$ denotes a scalar product.

We point out that no empty states are computed in the LL approach, and the techniques of the (static) density functional perturbation theory [33,36] are used: the projector on empty states is expressed as the difference between the unity operator and the projector on occupied states. Thus, only the occupied (valence and semicore) states are computed.

Moreover, we do not perform the computationally expensive inversion of the matrix $(\hbar\omega - \hat{\mathcal{L}})^{-1}$, and instead we use the Lanczos recursion algorithm [37]: the Liouvillian is applied to an initial perturbed state, and afterwards the result is iteratively continued yielding a series of Lanczos coefficients. Such a recursive procedure is independent of frequency. Using a small tridiagonal matrix composed of the Lanczos coefficients, the charge-density susceptibility for a given transferred momentum is obtained at any frequency by inverting this tridiagonal matrix for the desired frequency.

Details of the LL approach to EEL and IXS spectroscopies can be found in Refs. [8–10]. The limitations of the LL approach (as well as of the "conventional" TDDFT approach) in the TDDFT pseudopotential framework are dictated by the PP approximation and the accuracy of the exchange-correlation (XC) functionals to describe the semicore electrons that are excited in the extended energy range. They are discussed in Sec. III. To plot the loss function, $-\mathrm{Im}[\epsilon^{-1}(\mathbf{Q},\omega)]$, we added a small imaginary component to the frequency, $\omega \to \omega + i\eta$, leading to a Lorentzian broadening of the EEL spectra.

C. Spin-orbit coupling in the linear-response problem

The major contribution of relativistic effects comes from the core region and is accounted for in the construction of fully relativistic PP, by solving in the atom the relativistic Dirac-type KS equation for four-component spinor wave functions [38–42]. Nonrelativistic (Pauli-type) KS equations are then solved for valence electrons, the states of which are represented by two-component spinor wave functions by using the fully relativistic PP. This accounts for relativistic effects up to order α^2, where α is the fine-structure constant. The mass-velocity and the Darwin correction form the scalar-relativistic (SR) term, and SOC is due to the coupling of the spin and orbital angular momenta. The latter is particularly important in a heavy element like bismuth.

Formally, the time-independent Pauli-type KS equations read

$$\hat{H}^{\circ}\Psi^{\circ}_{n,\mathbf{k}} = \varepsilon^{\circ}_{n,\mathbf{k}}\Psi^{\circ}_{n,\mathbf{k}}, \tag{4}$$

and allow us to determine the ground-state two-component KS spinor wave functions $\Psi^{\circ}_{n,\mathbf{k}}$, energies $\varepsilon^{\circ}_{n,\mathbf{k}}$, charge density, and potentials. Here, n is the band index, and $\mathbf{k}$ is the point in the first BZ. The ground-state 2×2 Hamiltonian reads:

$$\hat{H}^{\circ} = \hat{T}^{\circ} + \hat{V}^{\circ}_{\mathrm{H}} + \hat{V}^{\circ}_{\mathrm{XC}} + \hat{V}^{\circ}_{\mathrm{loc}} + \hat{V}^{\circ}_{\mathrm{NL}}, \tag{5}$$

where $\hat{T}^{\circ}$ is the kinetic-energy operator for independent electrons, $\hat{V}^{\circ}_{\mathrm{H}}$ is the Hartree potential, $\hat{V}^{\circ}_{\mathrm{XC}}$ is the XC potential. The PP is described by two contributions: $\hat{V}^{\circ}_{\mathrm{loc}}$ is the local part of PP, and $\hat{V}^{\circ}_{\mathrm{NL}}$ is the nonlocal part, which is a sum of the SR and SOC contributions. The reader is referred to Ref. [42] for more details.

The time-dependent (TD) linearized Pauli-type KS equations are solved by mapping them onto a quantum Liouville equation for the response density matrix. For a monochromatic perturbation with wave vector **Q**, this equation in the frequency domain reads [8–10]

$$(\hbar\omega - \hat{\mathcal{L}}) \cdot \hat{\rho}'_{\mathbf{q}}(\omega) = [\hat{V}_{\mathrm{ext},\mathbf{q}}, \hat{\rho}^{\circ}], \tag{6}$$

where $\hat{\rho}'_{\mathbf{q}}(\omega)$ is the response density matrix operator. Equation (6) is defined in the two-component spinor space and, hence, it must be understood as a 2×2 matrix equation in such a space. The Liouvillian superoperator $\hat{\mathcal{L}}$ is defined through the "non-interacting" and "interacting" operators (see Refs. [8–10]). The former is defined as $\hat{H}^{\circ} - \varepsilon^{\circ}_{n,\mathbf{k}}$ and includes the SOC contribution explicitly [Eqs. (4) and (5)]. The interacting operator is defined as the response Hartree and XC potentials, which are expressed via the response charge density [i.e., the local in space element of $\hat{\rho}'_{\mathbf{q}}(\omega)$]. It is worth noting that the response charge density does not depend explicitly on SOC (i.e., does not contain any extra term due to SOC) but implicitly through the response KS spinor wave functions, coming from the self-consistent iterative solution of the quantum Liouville equation using the Lanczos recursive algorithm. We would like to stress that, in our study, both ground-state and TDDFpT equations have been solved including SOC *self-consistently*.

In this work we use fully relativistic norm-conserving PPs which we had developed for bismuth, using the method of Ref. [42] as implemented in the QUANTUM ESPRESSO package [43]. Neglecting SOC will mean that we neglect the SOC nonlocal term in $\hat{V}^{\circ}_{\mathrm{NL}}$ in Eq. (5) and keep only the SR term. In this case no splitting of the KS energy levels due to SOC is present. Obviously, in the SR approximation, usual KS wave functions are used instead of two-component spinors, and the nonrelativistic (TD) KS equations are solved.

D. Numerical details

The calculations have been performed by using density functional theory (DFT) [44,45] and TDDFpT in a plane-wave and PP framework using the QUANTUM ESPRESSO package [43]. The EEL spectra have been computed by using the turboEELS component [10], which contains the implementation of the LL approach to EEL and IXS spectroscopies.

Bismuth crystallizes in the A7 rhombohedral structure with two atoms in the primitive unit cell, and can be viewed as a Peierls distortion of the simple cubic lattice [46]. A detailed description of the geometry of Bi crystal can be found, e.g., in Refs. [47–50]. We have used fully relativistic norm-conserving PPs in the fully nonlocal (separable) form, in which the 5*d* semicore electrons were either included in the valence region [8,48], or frozen in the atomic core [49–51].

Spin-orbit coupling has been included in the calculations self-consistently as explained in Sec. II C. When including or neglecting SOC in the calculations, we have used the corresponding theoretical equilibrium lattice parameters optimized with or without SOC, respectively (see Table 5.1 of Ref. [8]).

We have considered two approximations for the XC energy; namely, the local density approximation (LDA) using Perdew–Zunger parametrization of the Ceperley–Alder functional [52], and the generalized gradient approximation (GGA) using Perdew–Burke–Ernzerhof parametrization [53]. Within each of these approximations we have used the corresponding theoretical equilibrium lattice parameters (see Table 5.1 of Ref. [8]).

The two-component KS spinor wave functions have been expanded in plane waves up to a kinetic-energy cutoff of 60 Ry, which was sufficient to obtain converged EEL spectra in the 0–100 eV range. The first BZ was sampled with a $14 \times 14 \times 14$ uniform **k** point mesh centered at the Γ point, and we have used a Methfessel–Paxton smearing scheme [54] with a broadening parameter of 0.02 Ry. The TDDFpT calculations have been performed by using an adiabatic approximation for the XC kernel (LDA or GGA). We used 2500 Lanczos iterations when the 5*d* semicore states were included in the valence region, and 8000 Lanczos iterations when they were frozen in the core region, as well as the extrapolation scheme [9,55]. To plot the EEL spectra we have used a Lorentzian smearing with a broadening of 0.035 Ry. The crystal and XC local field effects have been included.

III. ELECTRON ENERGY LOSS SPECTRA AT VANISHING TRANSFERRED MOMENTUM ($Q \to 0$)

This section is devoted to the study of the main factors which influence peak positions and intensities of the EEL spectrum calculated at vanishing transferred momentum. We analyze in particular the magnitude of the intensity integrated up to 20 eV. By decreasing importance, we find the inclusion of the 5*d* semicore states in the valence region (Sec. III A), local field effects (LFE), the SOC effect (Sec. III B), and the choice of the XC functional. The respective roles of LFE and of the XC functional are reported in the Supplementary Material [56].

A careful attribution of the peaks is performed in Table I, which is the main result of present section, and a detailed comparison is made with available experimental data (Sec. III C). We show, in particular, that the inclusion of the 5*d* semicore states in the valence region is crucial not only to reproduce the peaks between 20 and 30 eV and the broad structure between 40 and 100 eV, but also to obtain the correct position and shape of the bulk-plasmon peak at 14 eV. This analysis gives us confidence in the reliability of the predictions made in Sec. IV.

Only the [111] trigonal direction is investigated and the study of anisotropy is postponed to Sec. IV C.

A. Effect of 5*d* semicore states

The EEL spectra are widely different when 5*d* semicore states are included in the valence region or when they are frozen in the core (see Fig. 1). When 5*d* states are included in the valence region, the integrated intensity of the EEL spectrum over the range 0–500 eV is markedly increased by 60%.

Indeed, without an explicit account of the 5*d* semicore states in the valence region, the broad structure between 40 and 100 eV is not present in the spectrum, indicating that this structure is due to interband transitions from the 5*d* semicore states to higher conduction bands (see Table I and appendix for the details of the band structure). Neither are there peaks in the range 20–30 eV, which are due to interband transitions from the 5*d* semicore states to the lowest conduction bands. The authors of Ref. [57] have also shown that the EEL spectra of noble metals at high energies do have structures due to excitations

TABLE I. Peak positions (in eV) in the EEL spectrum of bulk Bi as obtained in this work for $Q \to 0$ in the trigonal direction and as measured in various experiments. The error bar in this work has been determined as the difference between peak positions computed within TDDFpT using the LDA and GGA XC functionals. The last column indicates origins of the peaks.

Peak	This work	Ref.[a]	Ref.[b]	Ref.[c]	Ref.[d]	Ref.[e]	Ref.[f]	Origin
1	5.8 ± 0.1	5	5	5.3 ± 0.2	5.3	5.6		Mixed
2			10	9.9 ± 0.2	9.5 ± 0.2		8.0 ± 0.5	Surface plasmon
3	14.0 ± 0.2	13.95 ± 0.15	14	14.7 ± 0.2	14.4 ± 0.2	14.1 ± 0.3	14.5 ± 0.5	Bulk plasmon
4	16.3 ± 1.0							Interband
5	22.6 ± 0.1	24.45 ± 0.2	24	24.8 ± 0.2	24.6		24.5 ± 0.5	Interband from 5*d* states
6	25.9 ± 0.2	27.3 ± 0.2	27		27.8	28	28.0 ± 0.5	Interband from 5*d* states
7			29	29 ± 0.2	29.7			
8							41.5 ± 0.5	
9	51 ± 4	52	52					Interband from 5*d* states
10							57.5 ± 0.5	

[a]Wehenkel and Gauthe [23].
[b]Gauthe and Wehenkel [22].
[c]Powell [17,18].
[d]Zacharias [21].
[e]Sueoka [20].
[f]Werner *et al.* [11].

from the semicore states. This is also true for some oxides, like titania and zirconia [58,59]. In cuprous oxide instead, the 3*s* and 3*p* semicore states are located at respectively −115 eV and −70 eV below the top of the valence band and their inclusion in the calculation has only a small effect on the plasmon position [60].

More remarkably, the inclusion of the 5*d* semicore states in the valence region turns out to be crucial to correctly find out the position and shape of the bulk plasmon, which is defined as a collective excitation of *valence* electrons. The bulk-plasmon peak occurs at 14 eV (see Table I, peak 3), whereas when 5*d* states are frozen in the core, it appears as a shoulder at 15.1 eV and the spectrum is dominated by a peak at 18.4 eV (which is otherwise not present in the EEL spectrum when 5*d* states are included in the valence region, see Fig. 1). We point out the fact that 5*d* states are localized and lie at low energies, −24.2 and −21.1 eV, and that the valence band structure is extremely well reproduced when 5*d* semicore states are frozen in core [51], but this turns out to be insufficient to correctly reproduce the dielectric function beyond 10 eV.

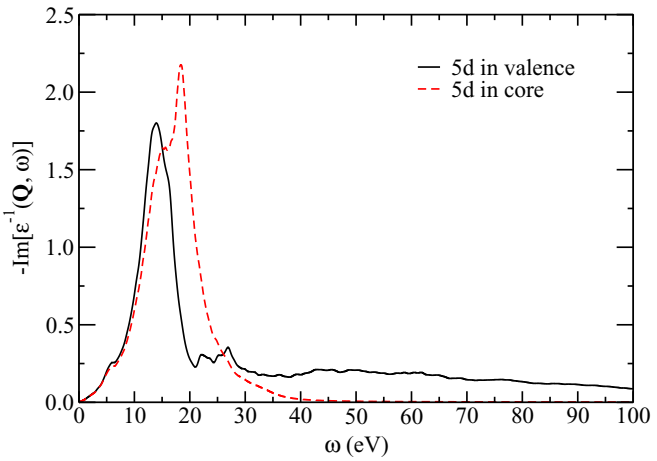

FIG. 1. EEL spectra of bulk Bi in the wide frequency range 0–100 eV computed for $Q \to 0$ in the trigonal direction within TDDFpT by using the LDA XC functional, including SOC, with 5*d* semicore states in the valence region or frozen in the core.

When 5*d* states are included in the valence region, the plasmon is redshifted by 1.1 eV and the shape of the spectrum is widely different, as for instance the integrated intensity from 0 up to 20 eV is decreased by 18.3%. In consequence, in the rest of the paper we show the results when 5*d* states are included in the valence region.

B. Effect of spin-orbit coupling

The effect of spin-orbit coupling is responsible for a very large splitting of the electronic energy states in Bi (see appendix) and, therefore, the EEL spectrum is expected to be sensitive to it. Although not as large as for the band structure, the effect of SOC on the EEL spectrum of Bi is significant, as can be seen in Fig. 2 [61]. When SOC is included, the position of the bulk-plasmon peak at 14 eV does not change while the integrated intensity up to 20 eV is decreased by 4.1%. We note that the change in the intensity of the plasmon peak in Bi due to SOC is similar to that in Pb (see Fig. 7.12 in Ref. [13]). Contrastingly, the peak at 5.8 eV is hardly affected by SOC. The peaks between 20 and 30 eV redshift with the inclusion of SOC and their intensity changes only slightly. Such a shift is due to the energy change of interband transitions, which is itself a consequence of the SOC-induced splitting of the 5*d* energy bands into O_4 and O_5 subshells [see Fig. 8(b)].

In the rest of this paper we present the results obtained when SOC was included in the calculations (except Sec. IV A, where we also show spectra without SOC).

C. Comparison with experiment in large energy range (up to 100 eV)

The EEL spectra calculated using the LDA and GGA XC functionals at vanishing transferred momentum agree

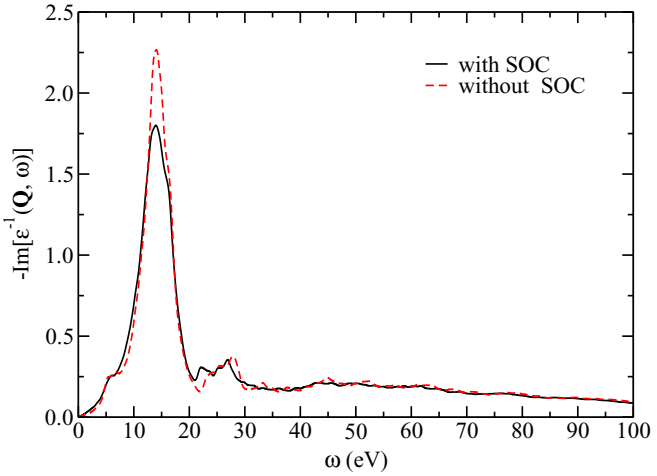

FIG. 2. EEL spectra of bulk Bi for $Q \to 0$ in the trigonal direction calculated with and without SOC at respective equilibrium lattice parameters using the LDA XC functional and including 5*d* semicore states in the valence region.

remarkably up to 100 eV with the experimental spectrum of Ref. [23] (see Fig. 3). We summarize all the structures in the EEL spectrum of Bi in Table I and define the error bar in this work as the difference between peak positions computed within TDDFpT by using the LDA and GGA XC functionals. A detailed comparison of theoretical results obtained with the LDA and GGA XC functionals can be found in the Supplementary Material [56].

Peak 1 at 5.8 eV is found in our calculations. This peak is observed as a shoulder in the experimental spectrum of Ref. [23] and was clearly resolved in other measurements [18,20–22]. As will be discussed later in Sec. IV A, our results suggest that this peak is not solely due to interband transitions, as believed before the present work: it is a resonant excitation between interband transitions from the occupied 6*p* states to empty 6*p* states, and the bulk plasmon, and thus, this excitation has a mixed character. The discrepancy with experiment on peak 1 is found to be in the range 0.2–0.8 eV (see Table I).

Remarkably, the position of the bulk plasmon at 14.0 eV coincides between theory (both LDA and GGA) and experiment (peak 3), and our results about Bi are an illustration of the success of TDDFT in predicting plasmon peak positions. Moreover, our calculations reveal the existence of an extra structure (peak 4), which was not resolved in the experiments. Such a structure is due to interband transitions and it appears as a shoulder when using LDA, while within GGA peaks 3 and 4 have very similar intensities and hence they form a unique broad structure. Such a plateau-like structure was not observed experimentally, and hence LDA shows a closer agreement to the experimental EEL spectrum in the range 10–20 eV.

Peaks 5 and 6 in the energy range between 20 and 30 eV are due to interband transitions from the 5*d* semicore states to the Fermi level and lowest empty states. These peaks show a redshift of 1.1–2.2 eV with respect to the experimental peak positions of Ref. [23] (see Table I), the scattering between the experimental results themselves amounting for the non-negligible value of ≈0.8 eV. The discrepancy between theory and experiment can be due to two factors: First, the imprecision of the energy position of the 5*d* semicore states within both LDA and GGA is in part responsible for the discrepancy, as for instance, with respect to the quasiparticle energies obtained in photoemission experiments, the discrepancy on the 5*d* semicore bands amounts to 2.8 eV (see appendix). TDDFT has thus a limited accuracy for interband transitions, because the positions of single-particle excitation energies depend on the LDA and GGA KS energies, and our study illustrates the need of *GW* corrections to blueshift this kind of excitations [62]. Second, one can expect a *semicore hole effect* in the 5*d* states caused by the interaction between the excited electron and the hole created in the 5*d* semicore state during the interband transition. This electron-hole interaction is usually treated with the Bethe–Salpeter approach [4,63,64] for valence electrons,

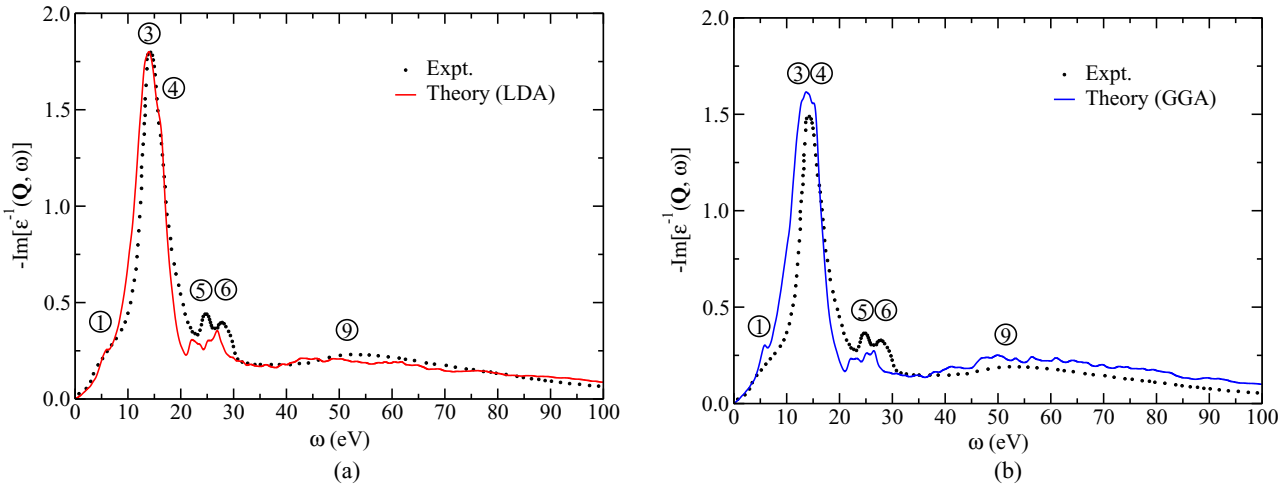

FIG. 3. Theoretical EEL spectrum of bulk Bi for $Q \to 0$ in the trigonal direction, calculated including SOC and using the (a) LDA XC functional, (b) GGA XC functional, and the experimental data in arbitrary units from Ref. [23]. The intensity at 35 eV of the experimental spectrum has been rescaled to the intensity at 35 eV of the theoretical spectrum to which it is compared. The numbering of the peaks and their values are indicated in Table I. The theoretical spectra are given in absolute units, and have been computed at their respective equilibrium lattice parameters.

or with the $Z + 1$ approximation for core excitations [65], and in both cases the excitation energy is redshifted.

Figure 3 shows that TDDFpT remarkably reproduces the broad structure extending between 40 and 100 eV (peak 9), thus validating our PP approximation for high-energy excitations [66]. The most recent EEL experiments on bulk bismuth [11] show that instead of one broad peak 9 (with a maximum intensity at around 51–52 eV), two peaks were found; namely, peaks 8 and 10 appearing at 41.5 and 57.5 eV, respectively, in contradiction with all other experiments and present theoretical study (see Table I). Such a discrepancy should be attributed to some artifacts in the experiments of Ref. [11]. New experiments with a higher accuracy are required to clarify whether there is one or two bands.

Moreover, we do not find the surface-plasmon peak 2 at ∼10 eV, which was observed in several experiments reported in Refs. [17,18,21,22], because we did not model a surface but a bulk material. Neither do we find peak 7 at ∼29 eV. In fact, the occurrence of some oxidation of bismuth can be suspected in the experiments in which this peak has been observed [17,18,21,22], because Bi_2O_3 has a peak at 29 eV, as was pointed out by Wehenkel and Gauthe [23]. Our calculations confirm that peak 7 does not come from the response of nonoxidized bulk Bi.

As can be seen from Table I, the comparison of TDDFpT results with the experimental ones in bismuth shows that the more collective the character of the excitation, the more precise the TDDFpT with respect to the experimental data.

Finally, it is worth noting that the RPA studies of EEL of Bi of Ref. [11] do not show as good agreement with the experimental EEL as our TDDFpT studies. In particular, in Fig. 26 of Ref. [11], the RPA loss function has intense spurious peaks in the range from 0 to 12 eV, which are not observed experimentally, the main plasmon peak position is underestimated by ∼2 eV, and the broad structure in the range from 40 to 100 eV decays too fast to zero intensity (probably because of not enough number of empty states included in the calculations). Our calculations using the LL approach to TDDFpT give instead a remarkable agreement with the experimental data of Ref. [23] thanks to the full TDDFpT level of approximation and, in particular, the broad structure decays correctly because of the (in principle) infinite number of empty states implicitly included in our calculations due to the use of techniques of density functional perturbation theory [33].

D. Real and imaginary parts of dielectric function

In this section we perform a more detailed comparison of the theoretical EEL spectrum within the LDA and the experimental EEL spectra of Bi (Refs. [21,23]) in the 0–35 eV range and discuss the origin of the peaks by considering the real and imaginary parts of the dielectric function, $\mathrm{Re}[\epsilon(\mathbf{Q},\omega)]$ and $\mathrm{Im}[\epsilon(\mathbf{Q},\omega)]$, for $Q \to 0$. We have computed the dielectric function according to the definition, $\epsilon(\mathbf{Q},\omega) \equiv 1/\epsilon^{-1}(\mathbf{Q},\omega)$, as explained in Ref. [10]. As shown in Fig. 4, overall there is a very good agreement between theoretical data of this work and the experimental ones. $\mathrm{Re}[\epsilon]$ and $\mathrm{Im}[\epsilon]$ follow closely the experimental data and capture all the prominent features.

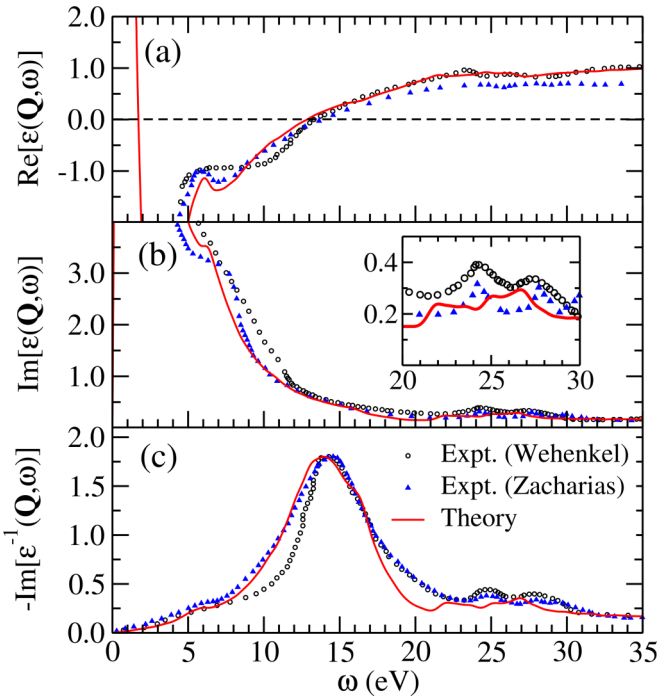

FIG. 4. (a) Real part of the dielectric function, $\mathrm{Re}[\epsilon(\mathbf{Q},\omega)]$, (b) Imaginary part of the dielectric function, $\mathrm{Im}[\epsilon(\mathbf{Q},\omega)]$, (c) Loss function, $-\mathrm{Im}[\epsilon^{-1}(\mathbf{Q},\omega)]$, for $Q \to 0$ in the trigonal direction as obtained from the experiments (Refs. [21,23]) and as calculated in this work within TDDFpT by using the LDA XC functional and including SOC. The inset in panel (b) contains a zoom of $\mathrm{Im}[\epsilon(\mathbf{Q},\omega)]$ in the region from 20 to 30 eV. The intensity of the experimental data was rescaled in the same way as in Fig. 3(a).

From Figs. 4(a) and 4(b) the information about the origin of the peaks can be obtained. Peak 1 in $\mathrm{Im}[\epsilon]$ was also found by Cardona and Greenaway at 5.3 eV in the optical absorption experiment [67] and it was attributed to the interband transitions from the occupied $6p$ states to empty $6p$ states. Since peak 1 is also present in the loss function [see Fig. 4(c)], it has been also attributed to interband transitions [18]. However, as will be shown in Sec. IV A, a strong dispersion with $\mathbf{Q}$ of peak 1 reveals that its origin is due in part to collective excitations. Therefore, we draw the conclusion that peak 1 has a *mixed* nature.

We would like to point out a remarkable agreement of the lower-energy part ($\omega < 14$ eV) of the plasmon peak (peak 3, Table I) with the experimental data of Ref. [21] [see Fig. 4(c)]. In the theoretical loss function the plasmon peak occurs [68] when $\mathrm{Re}[\epsilon] = 0.16$ and $\mathrm{Im}[\epsilon] = 0.49$, which is in good agreement with the results reported in Ref. [23]; namely, $\mathrm{Re}[\epsilon] = 0.06$ and $\mathrm{Im}[\epsilon] = 0.50$.

As was reported in Sec. III C and as can be seen in Fig. 4(c) in the theoretical EEL spectrum there is a shoulder at 16.3 eV (peak 4), which is due to interband transitions. This is so because in $\mathrm{Im}[\epsilon]$ there is a very weak shoulder at the same energy, which was not resolved in the experiments due to its low intensity.

It is known that, in general, a shift (from a fraction of 1 eV to several eV) can be observed between peaks due to interband transitions in $\mathrm{Im}[\epsilon]$ and $-\mathrm{Im}[\epsilon^{-1}]$ (see, e.g.,

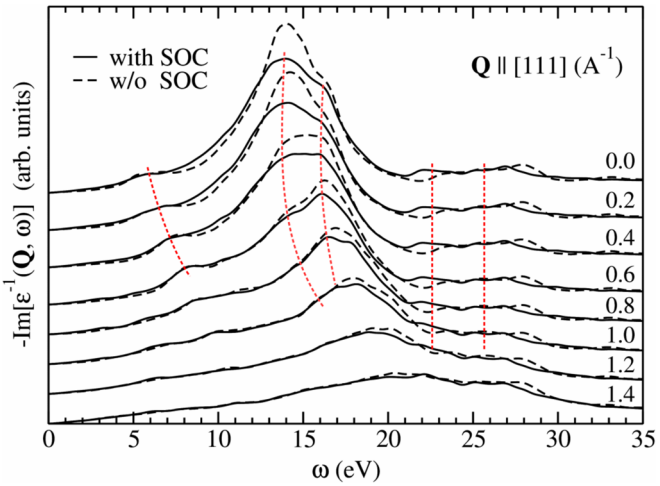

FIG. 5. EEL spectra with (solid lines) and without (dashed lines) SOC of bulk Bi at various values of **Q** along the [111] direction in framework of the reciprocal basis vectors of BZ ($Å^{-1}$). Curves have been shifted vertically for clarity. Calculations have been performed within TDDFpT using the LDA XC functional. Red dashed lines are guides for the eye showing the dispersion of the peaks.

Ref. [69]). However, such a shift in Bi is negligible for peaks 5 and 6. Indeed, these peaks in the EEL spectrum [Fig. 4(c)] coincide with the peaks in the imaginary part of the dielectric function [Fig. 4(b)], and hence they can unambiguously be attributed to interband transitions.

The remaining differences between theory and experiment in the real and imaginary parts of the dielectric function can be attributed to the fact that, first, the plasmon peak is very broad and, hence, it is not easy to find its maximum very precisely and thus, also the values of $\mathrm{Re}[\epsilon]$ and $\mathrm{Im}[\epsilon]$ satisfying the plasmon resonant condition, and second, the authors of Ref. [23] used the Kramers–Kronig analysis which introduces some uncertainty into the values of the dielectric function.

IV. ELECTRON ENERGY LOSS SPECTRA AT FINITE TRANSFERRED MOMENTA ($Q \neq 0$)

In this section we present results which are totally predictive. They have been obtained by using the best level of approximation which we could reach in this work; namely, TDDFpT including $5d$ semicore states in the valence region, including SOC, including LFE, and using the LDA XC functional. Moreover, in this section we analyze the effect of SOC and anisotropy at finite transferred momenta. Qualitatively similar results (not shown) were obtained by using the GGA XC functional, the geometrical effect discussed in the Supplementary Material [56] being the main source of difference between GGA and LDA.

A. Dispersion and nature of the peaks

Figure 5 shows the EEL spectra of Bi at various values of the transferred momentum **Q** along the [111] direction in the framework of the reciprocal basis vectors of BZ, i.e., along the trigonal axis (see, e.g., Ref. [48]). The analysis of the dispersion of the peaks complements our analysis of the origin of the peaks, which are summarized in the last column of Table I.

When the transferred momentum **Q** is increased, the bulk-plasmon peak 3 at 14 eV is blueshifted, showing a quadratic-like dispersion, while the peaks 5 and 6 in the 20–30 eV range do not change visibly their positions, which confirms that they are caused by the interband transitions from the $5d$ semicore states to the Fermi level and lowest empty states (see appendix for the initial and final electronic states, Figs. 8(a) and 8(b), respectively). The shoulder at 16.3 eV (peak 4) shows a weak dispersion with **Q**, confirming that it is due to interband transitions. When **Q** increases and reaches the critical value of $Q_c \approx 1.2\,Å^{-1}$, bulk-plasmon peak 3 merges with peaks 4, 5, and 6 which are due to the interband transitions, the spectrum becomes very broad and its intensity is decreased. Such a broadening of the EEL spectrum occurs because the energy of the plasmon is transferred to excitations of the electron-hole pairs [70].

As for peak 1 at 5.8 eV, it blueshifts largely when **Q** increases. This observation suggests that the $6p \rightarrow 6p$ interband transitions are mixing with the bulk-plasmon excitation, hence creating an excitation of a resonant mixed character. Thus, its attribution is reconsidered by our results and the peak should be regarded as having a mixed nature.

The EEL spectra at various values of **Q** were computed when SOC was included and neglected by using corresponding theoretical lattice parameters (see Table 5.1 of Ref. [8]). From Fig. 5 one can see that the effect of SOC is more pronounced for smaller values of **Q**, while for large **Q** it is less important. More investigation are needed in order to explain such a trend.

B. Dielectric function at finite Q

Figure 6 shows a comparison of the loss function, $-\mathrm{Im}[\epsilon^{-1}(\mathbf{Q}, \omega)]$, and the real and imaginary parts of the dielectric function, $\mathrm{Re}[\epsilon(\mathbf{Q}, \omega)]$ and $\mathrm{Im}[\epsilon(\mathbf{Q}, \omega)]$, respectively, for various values of the transferred momenta **Q** along the [111] direction. It can be seen that, for small **Q**, the loss function and the imaginary part of the dielectric function are very different, but for large **Q** they become almost identical. This is due to the fact that, for small transferred momenta **Q**, the long-range component of the Coulomb potential is important, whereas for large **Q** the short-range effects dominate [71,72]. The same trend has been observed by Weissker and co-workers in silicon (see Fig. 20 in Ref. [72]).

C. Effect of anisotropy

The anisotropy is determined by the electronic band structure and crystal local field effects [58,72]. We computed EEL spectra of Bi at several transferred momenta **Q** along the directions [111], [110], and [100] in the BZ (in the framework of the reciprocal basis vectors) within TDDFpT by using the LDA XC functional and including SOC. We find that the EEL spectra are anisotropic at large transferred momenta **Q**, as can be seen in Fig. 7. However, at small transferred momenta, e.g., $Q = 0.2\,Å^{-1}$, the anisotropy is very small. When Q is increased up to, e.g., $0.8\,Å^{-1}$ or larger, the anisotropy becomes very significant. At $Q = 0.2\,Å^{-1}$ and $Q = 0.8\,Å^{-1}$ peaks 5 and 6 due to the interband transitions from the $5d$ semicore

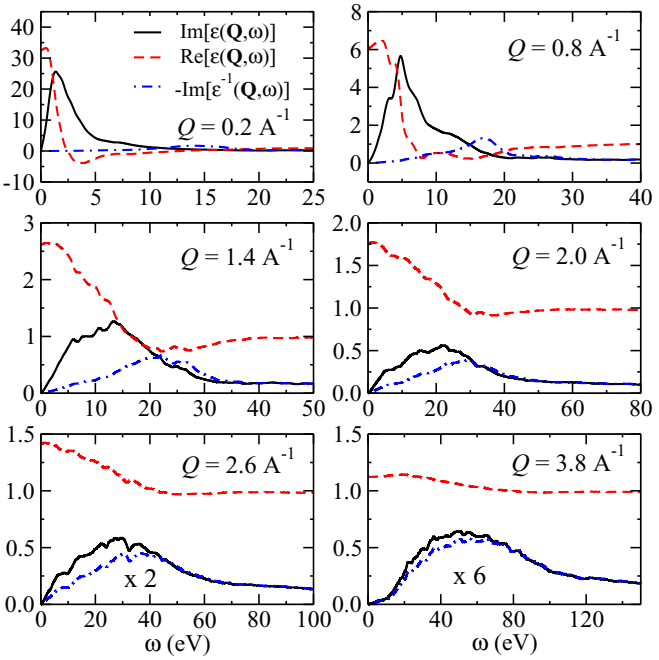

FIG. 6. Real and imaginary parts of the dielectric function, $\mathrm{Re}[\epsilon(\mathbf{Q},\omega)]$, $\mathrm{Im}[\epsilon(\mathbf{Q},\omega)]$, respectively, and the loss function, $-\mathrm{Im}[\epsilon^{-1}(\mathbf{Q},\omega)]$, at various values of the transferred momentum $\mathbf{Q}$ along the [111] direction calculated within TDDFpT using the LDA XC functional including SOC. In the lowest two panels, $\mathrm{Im}[\epsilon(\mathbf{Q},\omega)]$ and $-\mathrm{Im}[\epsilon^{-1}(\mathbf{Q},\omega)]$ were multiplied by a constant factor for better visibility.

states are isotropic, in contrast with the plasmon peak 3, peak 4 due to interband transitions, and peak 1 of the mixed nature. Also, we find that, by switching off SOC, the EEL spectra show qualitatively the same anisotropic behavior with increasing Q as when SOC is included in the calculations [8].

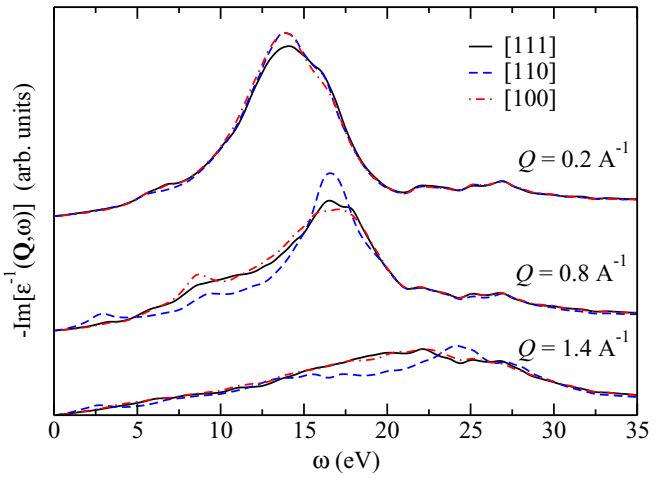

FIG. 7. EEL spectra computed for several values of $\mathbf{Q}$ along the [111], [110], and [100] directions in BZ (in framework of the reciprocal basis vectors), within TDDFpT by using the LDA XC functional and including SOC. Curves have been shifted vertically for clarity.

V. CONCLUSIONS

We have presented a theoretical study of the EEL spectra of bulk Bi at vanishing and finite transferred momenta. The study has been done by using our recently developed Liouville–Lanczos approach to EEL and IXS spectroscopies, which allowed us to study energy losses up to 100 eV, a wide excitation energy range of interest in bismuth. Spin-orbit coupling has been included self-consistently in our calculations.

The EEL spectrum at vanishing transferred momentum have been found to be in remarkable agreement with available experimental data. Including $5d$ states in the calculations is crucial, as we have shown that the dielectric function is not correctly described for energies larger than 10 eV when they are frozen in the core. Our calculations reveal the presence of interband transitions at 16.3 eV, which were previously not identified because they were not distinguished from the bulk plasmon. A careful experimental analysis of the relative dispersion of the bulk plasmon and of the shoulder at 16.3 eV, as done in present theoretical work, is called for. We have presented the dependence of the dielectric function and of the loss function on the value of the transferred momentum, and have studied the influence of various effects such as SOC, crystal and exchange-correlation local fields, and anisotropy.

Our results complement the lack of experimental data at finite transferred momenta, and we have shown in particular that, for values of $\mathbf{Q}$ larger than ≈ 1.2 Å^{-1}, the plasmon decays into electron-hole pairs. Finally, the peak at 5.8 eV is attributed by the present work to a resonant coupling between $6p \rightarrow 6p$ interband transitions and the bulk plasmon. Measurements of the EEL spectra of bulk Bi at vanishing and finite transferred momenta are called for.

ACKNOWLEDGMENTS

We thank L. Reining, F. Sottile, J. Sjakste, and A. Dal Corso for valuable discussions. The calculations were performed by using the QUANTUM ESPRESSO package [43]. Support from the ANR (France) (Project No. PNANO ACCATONE), from the DGA (France), and from the EU Centre of Excellence "MaX - Materials Design at the Exascale" (Project No. 676598) is gratefully acknowledged. Computer time was granted by École Polytechnique through the LLR-LSI project, by GENCI (France) (Project No. 2210), and CINECA (Italy) (Project No. ISCRA C).

APPENDIX: KOHN-SHAM BAND STRUCTURE

The electronic configuration of Bi consists of $6s^2 6p^3$ valence electrons, $5d^{10}$ semicore electrons, and the lower-lying electrons forming the core. In the DFT and tight-binding calculations the $5d$ semicore electrons can be treated either on the same footing as $6s$ and $6p$ valence electrons [48,73] or frozen in the core [49,50,74–78]. In Ref. [48] it was reported, however, that the inclusion of the $5d$ semicore electrons in PP improves its transferability properties.

The KS band structure of Bi along some high-symmetry directions in the BZ is illustrated in Fig. 8, which was calculated within DFT-LDA with and without SOC. The KS band structure within DFT-GGA can be found in Ref. [8]. Here we

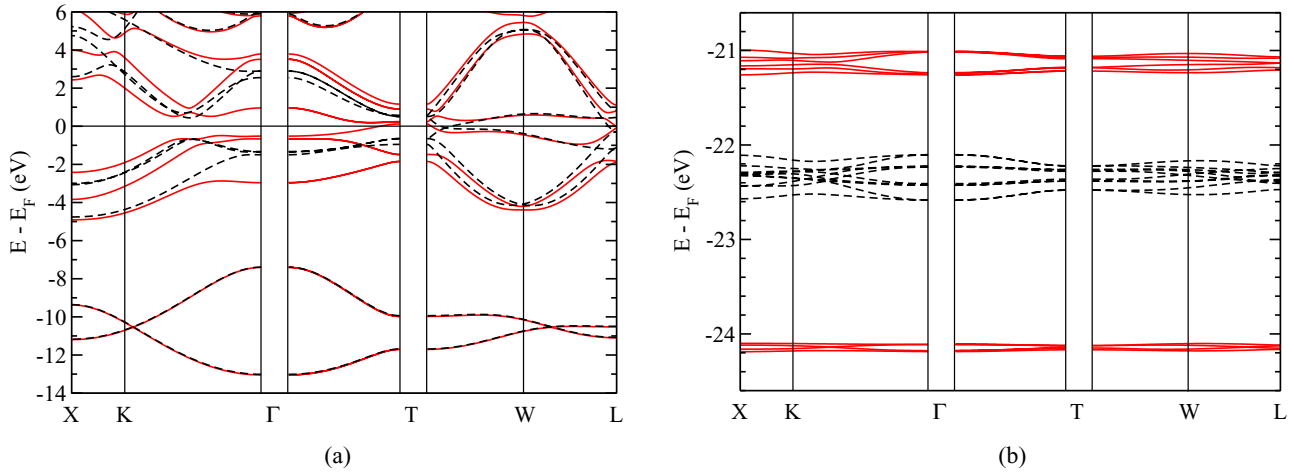

FIG. 8. Kohn–Sham band structure of Bi with SOC (red solid lines) and without SOC (black dashed lines) calculated within DFT-LDA. (a) Valence 6*s* bands, valence and conduction 6*p* bands, and higher-energy bands. (b) Semicore 5*d* bands. Fermi level is at zero energy.

present the DFT-LDA KS band structure for the analysis of the EEL spectra within TDDFpT by using the LDA XC functional.

The effect of SOC on the band structure of Bi is crucial. The first study showing this effect is Ref. [75]. Here we summarize the results [8] which are needed for discussions in this work. When SOC is not included in the calculations, Bi turns out to be metallic, because there is an artificial crossing of bands at the Fermi level [see Fig. 8(a)]. The semimetallic character of the band structure is entirely due to SOC, which leads to large splittings of all energy bands except *s* bands [e.g., 6*s* bands in Fig. 8(a)]. The large splitting of 6*p* bands, in turn, leads to an extremely small overlap around the Fermi level between the lowest conduction band and the highest valence band (see Tables 5.2 and 5.3 in Ref. [8]), resulting in a Fermi surface consisting of one hole pocket at the T point and three equivalent electron pockets at the L points [48,75,76]. The localized 5*d* semicore states lie more deeply and also split due to SOC forming two groups of bands—O_4 and O_5 subshells [see Fig. 8(b)]. The 5*d* semicore bands show very weak dispersion with respect to valence and conduction bands.

Both in DFT-LDA and DFT-GGA the 5*d* semicore states appear on average at -24.2 and -21.1 eV when SOC is included, and in the range $[-22.2; -22.6]$ eV without SOC [see Fig. 8(b)]. The photoemission data on Bi indicate that the binding-energy values of the O_4 and O_5 subshells relative to the Fermi level, which is taken to be zero, are -26.5 ± 0.5 and -24.4 ± 0.6 eV, respectively [79]. This average discrepancy of 2.8 eV between LDA (GGA) and photoemission data in the description of the O_4 and O_5 subshells of the 5*d* semicore shell is due to the limited accuracy of our approximations of the XC energy, and a possible need to account for quasiparticle corrections to the KS band structure by using the GW method [80,81], which has been recently applied to Bi including SOC [82]. Consequently, this has an effect on the peak positions in the EEL spectra of Bi, which are due to transitions from the 5*d* semicore states to unoccupied states.

[1] R. F. Egerton, *Electron Energy-Loss Spectroscopy in the Electron Microscope*, 2nd ed. (Plenum, New York and London, 1996).

[2] E. Runge and E. K. U. Gross, Phys. Rev. Lett. **52**, 997 (1984).

[3] E. K. U. Gross, J. F. Dobson, and M. Petersilka, *Density Functional Theory of Time-Dependent Phenomena*, Topics in Current Chemistry (Springer-Verlag, Berlin, 1996).

[4] G. Onida, L. Reining, and A. Rubio, Rev. Mod. Phys. **74**, 601 (2002).

[5] J. A. Soininen, A. L. Ankudinov, and J. J. Rehr, Phys. Rev. B **72**, 045136 (2005).

[6] Y. Joly, Phys. Rev. B **63**, 125120 (2001).

[7] D. Cabaret, N. Emery, C. Bellin, C. Herold, P. Lagrange, F. Wilhelm, A. Rogalev, and G. Loupias, Phys. Rev. B **87**, 075108 (2013).

[8] I. Timrov, Ph.D. thesis, École Polytechnique, France, 2013.

[9] I. Timrov, N. Vast, R. Gebauer, and S. Baroni, Phys. Rev. B **88**, 064301 (2013); **91**, 139901 (2015).

[10] I. Timrov, N. Vast, R. Gebauer, and S. Baroni, Comput. Phys. Commun. **196**, 460 (2015).

[11] W. Werner, K. Glantschnig, and C. Ambrosch-Draxl, J. Phys. Chem. Ref. Data **38**, 1013 (2009).

[12] K. Glantschnig and C. Ambrosch-Draxl, New J. Phys. **12**, 103048 (2010).

[13] X. Zubizarreta, Ph.D. thesis, Universidad del Pais Vasco, 2012.

[14] X. Zubizarreta, V. M. Silkin, and E. V. Chulkov, Phys. Rev. B **87**, 115112 (2013).

[15] X. Zubizarreta, V. M. Silkin, and E. V. Chulkov, Phys. Rev. B **90**, 165121 (2014).

[16] J.-P. Issi, Aust. J. Phys. **32**, 585 (1979).

[17] C. J. Powell, Proc. Phys. Soc., London **76**, 593 (1960).

[18] C. J. Powell, Phys. Rev. Lett. **15**, 852 (1965).

[19] C. J. Powell, Phys. Rev. **175**, 972 (1968).

[20] O. Sueoka, J. Phys. Soc. Jpn. **20**, 2203 (1965).

[21] P. Zacharias, Opt. Commun. **8**, 142 (1973).

[22] B. Gauthe and C. Wehenkel, Phys. Lett. A **39**, 171 (1972).

[23] C. Wehenkel and B. Gauthé, Solid State Commun. **15**, 555 (1974).

[24] M. S. Sander, R. Gronsky, Y. M. Lin, and M. S. Dresselhaus, J. Appl. Phys. **89**, 2733 (2001).

[25] T. W. Cornelius, Ph.D. thesis, Ruperto-Carola University of Heidelberg, 2006.

[26] Y. W. Wang, J. S. Kim, G. H. Kim, and K. S. Kim, Appl. Phys. Lett. **88**, 143106 (2006).

[27] Y. Wang, J. S. Kim, J. Y. Lee, G. H. Kim, and K. S. Kim, Chem. Mater. **19**, 3912 (2007).

[28] N. Jiang, D. Su, J. C. H. Spence, S. Zhou, and J. Qiu, Solid State Commun. **149**, 111 (2009).

[29] M. Li, Z. Wang, R. Q. Zhang, and A. Soon, Solid State Commun. **152**, 1564 (2012).

[30] L. V. Hove, Phys. Rev. **95**, 249 (1954).

[31] R. Car, E. Tosatti, S. Baroni, and S. Leelaprute, Phys. Rev. B **24**, 985 (1981).

[32] M. S. Hybertsen and S. G. Louie, Phys. Rev. B **35**, 5585 (1987).

[33] S. Baroni, S. de Gironcoli, A. Dal Corso, and P. Giannozzi, Rev. Mod. Phys. **73**, 515 (2001).

[34] O. B. Malcioglu, R. Gebauer, D. Rocca, and S. Baroni, Comput. Phys. Commun. **182**, 1744 (2011).

[35] X. Ge, S. J. Binnie, D. Rocca, R. Gebauer, and S. Baroni, Comput. Phys. Commun. **185**, 2080 (2014).

[36] S. Baroni, P. Giannozzi, and A. Testa, Phys. Rev. Lett. **58**, 1861 (1987).

[37] Y. Saad, *Iterative Methods for Sparse Linear Systems*, 2nd ed. (SIAM, Philadelphia, 2003).

[38] L. Kleinman, Phys. Rev. B **21**, 2630 (1980).

[39] G. B. Bachelet and M. Schlüter, Phys. Rev. B **25**, 2103 (1982).

[40] L. A. Hemstreet, C. Y. Fong, and J. S. Nelson, Phys. Rev. B **47**, 4238 (1993).

[41] G. Theurich and N. A. Hill, Phys. Rev. B **64**, 073106 (2001).

[42] A. Dal Corso and A. Mosca Conte, Phys. Rev. B **71**, 115106 (2005).

[43] P. Giannozzi, S. Baroni, N. Bonini, M. Calandra, R. Car, C. Cavazzoni, D. Ceresoli, G. Chiarotti, M. Cococcioni, I. Dabo *et al.*, J. Phys.: Condens. Matter **21**, 395502 (2009).

[44] P. Hohenberg and W. Kohn, Phys. Rev. **136**, B864 (1964).

[45] W. Kohn and L. Sham, Phys. Rev. **140**, A1133 (1965).

[46] R. Peierls, *More Surprises in Theoretical Physics* (Princeton University Press, Princeton, 1991).

[47] R. J. Needs, R. M. Martin, and O. H. Nielsen, Phys. Rev. B **33**, 3778 (1986).

[48] I. Timrov, T. Kampfrath, J. Faure, N. Vast, C. R. Ast, C. Frischkorn, M. Wolf, P. Gava, and L. Perfetti, Phys. Rev. B **85**, 155139 (2012).

[49] M. Markov, J. Sjakste, G. Fugallo, L. Paulatto, M. Lazzeri, F. Mauri, and N. Vast, Phys. Rev. B **93**, 064301 (2016).

[50] M. Markov, Ph.D. thesis, Université Paris-Saclay, École Polytechnique, France, 2016.

[51] The pseudopotential with 5*d* electrons frozen in the core was optimized (Refs. [49,50]) to reproduce the DFT-LDA electronic band structure obtained in Refs. [8,48]. Dispersion of acoustic phonons of bismuth and thermal conductivity calculated with that pseudopotential were found in very good agreement with experimental data (Refs. [49,50]).

[52] J. P. Perdew and A. Zunger, Phys. Rev. B **23**, 5048 (1981).

[53] J. P. Perdew, K. Burke, and M. Ernzerhof, Phys. Rev. Lett. **77**, 3865 (1996).

[54] M. Methfessel and A. T. Paxton, Phys. Rev. B **40**, 3616 (1989).

[55] D. Rocca, R. Gebauer, Y. Saas, and S. Baroni, J. Chem. Phys. **128**, 154105 (2008).

[56] See Supplemental Material at http://link.aps.org/supplemental/10.1103/PhysRevB.95.094301 for a discussion about the local field effects at $Q \to 0$ and at finite Q, and the effect of the exchange-correlation functional at $Q \to 0$.

[57] A. Alkauskas, S. D. Schneider, C. Hébert, S. Sagmeister, and C. Draxl, Phys. Rev. B **88**, 195124 (2013).

[58] N. Vast, L. Reining, V. Olevano, P. Schattschneider, and B. Jouffrey, Phys. Rev. Lett. **88**, 037601 (2002).

[59] L. K. Dash, N. Vast, P. Baranek, M.-C. Cheynet, and L. Reining, Phys. Rev. B **70**, 245116 (2004).

[60] L. K. Dash, F. Bruneval, V. Trinité, N. Vast, and L. Reining, Comput. Mater. Sci. **38**, 482 (2006).

[61] It is worth noting the the EEL spectrum computed by neglecting SOC and using the lattice parameters optimized with or without SOC are almost identical. Hence, the geometrical effect on the EEL spectrum on the large energy scale due to the SOC-induced change in the lattice parameters is negligible.

[62] F. Aryasetiawan and O. Gunnarsson, Rep. Prog. Phys. **61**, 237 (1998).

[63] V. Olevano and L. Reining, Phys. Rev. Lett. **86**, 5962 (2001).

[64] J. A. Soininen, and E. L. Shirley, Phys. Rev. B **61**, 16423 (2000).

[65] G. Duscher, R. Buczko, S. Pennycook, and S. Pantelides, Ultramicroscopy **86**, 355 (2001).

[66] It is worth noting that it would be cumbersome to compute this broad structure with the conventional TDDFT approach (Ref. [4]), because one would require a huge number of empty states in order to converge the EEL spectrum over such a wide energy range. However, with the LL approach no empty states are calculated and, thus, such a broad structure can be easily computed.

[67] M. Cardona and D. L. Greenaway, Phys. Rev. **133**, A1685 (1964).

[68] H. Mendlowitz, J. Opt. Soc. Am. **50**, 739 (1960).

[69] A. Alkauskas, S. Schneider, S. Sagmeister, C. Ambrosch-Draxl, and C. Hébert, Ultramicroscopy **110**, 1081 (2010).

[70] G. D. Mahan, *Many-Particles Physics*, 2nd ed. (Plenum Press, New York, 1975).

[71] H.-C. Weissker, J. Serrano, S. Huotari, F. Bruneval, F. Sottile, G. Monaco, M. Krisch, V. Olevano, and L. Reining, Phys. Rev. Lett. **97**, 237602 (2006).

[72] H.-C. Weissker, J. Serrano, S. Huotari, E. Luppi, M. Cazzaniga, F. Bruneval, F. Sottile, G. Monaco, V. Olevano, and L. Reining, Phys. Rev. B **81**, 085104 (2010).

[73] G. Gutiérrez, E. Menéndez-Proupin, and A. Singh, J. Appl. Phys. **99**, 103504 (2006).

[74] X. Gonze, J.-P. Michenaud, and J.-P. Vigneron, Phys. Scr. **37**, 785 (1988).

[75] X. Gonze, J.-P. Michenaud, and J.-P. Vigneron, Phys. Rev. B **41**, 11827 (1990).

[76] J. H. Xu, E. G. Wang, C. S. Ting, and W. P. Su, Phys. Rev. B **48**, 17271 (1993).

[77] Y. Liu and R. E. Allen, Phys. Rev. B **52**, 1566 (1995).

[78] B. Arnaud and Y. Giret, Phys. Rev. Lett. **110**, 016405 (2013).

[79] J. A. Bearden and A. F. Burr, Rev. Mod. Phys. **39**, 125 (1967).

[80] L. Hedin, Phys. Rev. **139**, A796 (1965).

[81] M. van Schilfgaarde, T. Kotani, and S. Faleev, Phys. Rev. Lett. **96**, 226402 (2006).

[82] I. Aguilera, C. Friedrich, and S. Blügel, Phys. Rev. B **91**, 125129 (2015).